

Source of the 6 February 2013 Mw 8.0 Santa Cruz Islands Tsunami

F. Romano¹, I. Molinari¹, S. Lorito¹, and A. Piatanesi¹

¹Istituto Nazionale di Geofisica e Vulcanologia, Via di Vigna Murata 605, 00143, Rome,
Italy

Corresponding author: Fabrizio Romano (fabrizio.romano@ingv.it)

*February 2015, Submission to NHESS (special issue “Progress in tsunami science in light
of the 2004 and 2011 tsunamis”)*

Revised on May 2015

18 **Abstract**

19 On February 6, 2013 an M_w 8.0 subduction earthquake occurred close to Santa Cruz Islands
20 at the transition between the Solomon and the New Hebrides Trench. The ensuing tsunami
21 caused significant inundation on the closest Nendo Island. The seismic source was studied
22 with teleseismic broadband P waves inversion optimized with tsunami forward modeling at
23 DART buoys (Lay et al., 2013), and with inversion of teleseismic body and surface waves
24 (Hayes et al., 2014). The two studies also use different hypocenters and different planar fault
25 models, and found quite different slip models. In particular, Hayes et al. (2014) argued for
26 an aseismic slip patch SE from the hypocenter. We here develop a 3D model of the fault
27 surface from seismicity analysis and retrieve the tsunami source by inverting DART and
28 tide-gauge data. Our tsunami source model features a main slip patch (peak value of ~ 11 m)
29 SE of the hypocentre, and reaching ~~to~~ the trench. The rake direction is consistent with the
30 progressively more oblique plate convergence towards the Solomon trench. The tsunami
31 source partially overlaps the hypothesized aseismic slip area, which then might have slipped
32 coseismically.

33

1 Introduction

On February 6, 2013 an M_w 8.0 earthquake occurred in the Pacific Ocean nearby the archipelago of Santa Cruz Islands. The hypocenter (165.138°E 10.738°S , depth ~ 29 km, USGS, <http://comcat.cr.usgs.gov/earthquakes/eventpage/usc000f1s0#summary>) is located at the subduction interface between the Australia and the Pacific plates, 76 km West from Lata, the main city of Nendo Island (Fig. 1 and Fig. 2).

This earthquake, the largest in 2013, occurred on a complex section of the Australia-Pacific plate boundary at the northern end of the New Hebrides trench (Hayes et al., 2012), nearby a short segment of dominantly strike-slip plate motion that marks the transition between Vanuatu and the Solomon Islands subduction zones. This segment is characterized by a complex tectonic regime that becomes progressively more oblique westward as revealed by the focal mechanisms of the local seismicity (Fig. 1). In this region the relative convergence velocity between Australia and Pacific plates is ~ 9.4 cm/yr (DeMets et al., 2010).

The Santa Cruz Islands earthquake generated a tsunami that struck the Nendo Island, in particular the city of Lata with waves higher than 1 m. Several runup and flowdepth measurements have been collected during a field survey conducted on some islands of the archipelago a few days after the earthquake (Fritz et al., 2014), reporting maximum tsunami wave heights of about 11 m in the western part of the Nendo Island. In addition, the tsunami propagated in the Pacific Ocean, also reaching the coasts of Hawaii (Lay et al., 2013).

Seismic and tsunami source of this earthquake have been previously studied with different methodologies (Lay et al., 2013; Hayes et al., 2014a), highlighting some differences between the resulting models in terms of both slip patches positions and slip amplitude. Hayes et al. (2014a) studied the Santa Cruz Islands earthquake by inverting teleseismic body and surface waves; Lay et al. (2013) performed a teleseismic broadband P waves inversion optimized with tsunami forward modelling at DART buoys. These studies used different hypocenters and different planar fault models; in particular, Lay et al. (2013) adopted both hypocenter and fault plane shallower than those used by Hayes et al. (2014a). The best-fitting source model in Hayes et al. (2014a, hereinafter HA14) has a main patch of slip centred around the hypocenter with a maximum slip of about 4 m and a second smaller patch located SE of the Nendo Island and characterized by relatively low slip (~ 0.5 m). On the other hand, the source model in Lay et al. (2013, hereinafter LA13) features two patches with slip larger than 10 m; the first patch is located around the hypocenter, whereas the second one is shallower and located SE of the hypocenter. The surface projection of the slip in LA13 is roughly consistent with the HA14 patches even if they are at different depths

68 (and featuring quite different slip values), because of the different fault planes used. In
69 addition, the LA13 source model is more efficient in terms of tsunami waves excitation than
70 that of HA14 and quite well predicts the tsunami observations recorded at the DART buoys.
71 The usual pattern of the aftershocks distribution following a great subduction earthquake
72 should show a large number of events occurring— ~~along the unbroken portion of the~~
73 ~~subduction interface at the subduction interface not dislocated~~, eventually also bordering the
74 broken asperities (Aki, 1979). On the other hand, as already extensively discussed (Hayes et
75 al., 2014a; Lay et al., 2013), after the 2013 February 6 event, very few events were located
76 along the subduction interface. Furthermore, most of early aftershocks in the epicentral area
77 (~200 events within 48 hours from the mainshock, <http://earthquake.usgs.gov/regional/neic/>)
78 showed strike-slip and normal mechanism, including two earthquakes with $M_w > 7$ occurred
79 in the upper crust portion of the Pacific plate and in the outer-rise trench region. Hayes et al.
80 (2014a) proposed a block-like motion behaviour of the Pacific upper plate to explain these
81 observations. In particular, they argued that a large number of anomalous right-lateral strike-
82 slip events located southeast of Nendo Island were triggered by significant aseismic slip
83 along a portion of the megathrust south-eastward from the epicentral area. However, LA13
84 model features significant coseismic slip on this portion of the fault; these differences may
85 be due to the different data used and/or to the different fault models adopted in the
86 inversions.

87 Here we study the coseismic tsunami source of the Santa Cruz Islands earthquake by
88 inverting the available tsunami waveforms. We compute the Green's functions at the DART
89 buoys and tide gauges using a 3D fault model that honours the complex geometry of the
90 subduction interface. After retrieving the tsunami source model, we discuss it in comparison
91 with LA13 and HA14 source models.

92
93

94 **2 Tsunami Data and Fault model**

95 The tsunami generated by the Santa Cruz Islands earthquake propagated both in the North
96 and South Pacific Ocean and it has been observed in the open sea at several DART buoys
97 and at some tide gauges located along the coasts of Solomon and Fiji Islands. We select 5
98 DART buoys (52403, 52406, 51425, 55012, and 55023,
99 <http://www.ndbc.noaa.gov/dart.shtml>) and 3 tide gauges (Lata Wharf, Honiara, and Lautoka,
100 <http://www.ioc-sealevelmonitoring.org>) that distinctly recorded a tsunami signal and that
101 allows a good azimuthal coverage (Fig. 2, further details in Supplementary Material). Before

using the tsunami data in the inversion, we remove the tide from the original signals by using a robust LOWESS procedure (Barbosa et al., 2004).

The fault model geometry can greatly influence the results of source inversion. Adopting a fault geometry that honours the complexities of the subduction interface then may help to reduce the epistemic uncertainties associated to forward modelling (Romano et al., 2014). This is particularly true for earthquakes of this size occurring in subduction zones characterized by strong variations of strike and/or dip (e.g. Hayes et al., 2014b), even more so in complex tectonic environments like the Santa Cruz Islands region.

Thus, analysing the aftershocks distribution occurred after the February 6 mainshock, the local seismicity, and considering the rupture area expected for a M8 event, we built a 3D non-planar fault model with variable strike and dip angles in order to account for such geometrical complexities of the subduction interface on both the New Hebrides and Solomon trenches (Bird, 2003). In particular, we selected from the EHB global relocation earthquake catalogue (<http://www.isc.ac.uk/ehbulletin/>; Engdahl et al., 1998) the events occurred in the area covered by the aftershocks of the Santa Cruz Islands earthquake and having $M > 4.5$. After removing those ones relatively distant from the trench (distance > 200 km), we drew sections perpendicular to the trench at a distance of ~ 20 km each (measured along the trench) projecting on them all the events in a neighbourhood of 30 km. We obtained several 2D profiles by fitting the data of each section. The resulting suite of 2D profiles was then further interpolated using CUBIT software (<http://cubit.sandia.gov>) in order to obtain a 3D fault model, meshed into 45 quadrangular patches (9 along strike and 5 along dip, Figs. 2, S1, S2) with an average size of about 20×20 km. Our final fault model is consistent with the northern interface of Vanuatu slab model in Slab1.0 (Hayes et al., 2012, <http://earthquake.usgs.gov/data/slab/>) and extends both up to the trench and in the north-west direction for ~ 40 - 60 km. The dimensions of the resulting fault are ~ 180 km along strike and ~ 90 km along dip (see Figs. 2, S1, S2).

3 Green's functions and Inversion scheme

The tsunami Green's functions are computed by means of NEOWAVE, a nonlinear dispersive model for tsunami waves propagation (Yamazaki et al., 2009; Yamazaki et al., 2011). The initial conditions for tsunami propagation are analytically computed (further details in Meade, 2007; Romano et al., 2012) and they also include the contribution of the

135 coseismic horizontal deformation in the region of steep bathymetric slopes (Tanioka and
136 Satake, 1996).

137 For tsunami modelling at the DART buoys we use a bathymetric grid with a spatial
138 resolution of 1 arc-min, whereas the Green's functions at the tide gauges are computed on a
139 grid of 30 arc-sec in order to better model the nearshore tsunami propagation. The
140 bathymetric data set used for tsunami simulations is SRTM30+
141 (http://topex.ucsd.edu/WWW_html/srtm30_plus.html), which is resampled for the grid of 1
142 arc-min.

143 We solve the inverse problem by using the Heat Bath algorithm, which is a particular
144 implementation of the Simulated Annealing technique (Rothman, 1986). For tsunami
145 waveforms we use a cost function that is sensitive both to amplitude and phase matching
146 (Spudich and Miller, 1990). This approach and the a-posteriori analysis of the explored
147 ensemble of models have been extensively tested and used in previous works (detailed
148 description of the method can be found for example in Piatanesi and Lorito, 2007; Lorito et
149 al., 2011; Romano et al., 2014 and references therein).

150 We make some a-priori assumptions on ranges for slip and rake: for each subfault the slip
151 can vary from 0 to 15 m at 0.5 m steps, whereas the rake can vary from 40° to 100° at 5°
152 steps on 3 large blocks (see Fig. S1). Furthermore, we assume a circular rupture front that
153 propagates with a rupture velocity of 1.5 km/s (Lay et al., 2013).

154 In each inversion we retrieve the best fitting slip distribution model, the average model
155 obtained by the ensemble of models that fits the data fairly well, and the standard deviations
156 for each inferred model parameter (e.g. Table S3).

157

158 **3.1 Checkerboard resolution test**

159 We evaluate the resolving power of the inversion setup (i.e., fault parameterization and
160 instrumental azimuthal coverage) by means of a synthetic test. In particular, we attempt to
161 reproduce a slip distribution assuming a target checkerboard pattern with slip values of 0 and
162 10 m on alternating subfaults (Fig. 3a). In addition, we set the target rake angle on the
163 easternmost, middle, and westernmost blocks equal to 90°, 70°, and 50°, respectively. We
164 invert the synthetic tsunami waveforms resulting from the target slip pattern by following
165 the same inversion procedure described above. Synthetic tsunami waveforms are corrupted
166 by adding Gaussian random noise with a variance that is the 10% of the clean waveform
167 amplitude variance. The average model for slip distribution (Fig. 3b) reproduces very well
168 the checkerboard target (Fig. 3a). We observe that the maximum differences between the

target and the retrieved slip models are smaller than 1 m **on average** (absolute value), **with a maximum discrepancy of ~2.5 m along the deepest subfaults**. The chosen inversion setup is also well calibrated to recover the target slip direction (i.e., the rake angle) on the fault plane, and the comparison between the synthetic and predicted tsunami waveforms shows an excellent agreement (Fig. S3). **We point out that such a checkerboard test only allows the analysis of the resolution that is granted in principle by the inversion setup (model geometry, station distribution)**. Eventual epistemic uncertainty that is inherent in the numeric tsunami model and/or due to the inaccuracy of the bathymetric model cannot be quantified in this way. Accordingly, the uncertainty associated to the average slip model (Table S3) is addressed through the analysis of the model ensemble, as discussed in the previous section.

4 Source of the 2013 Santa Cruz Islands tsunami

We use the same inversion scheme, fault parameterization, and set of DART buoys and tide gauges data used for the checkerboard test to retrieve the coseismic tsunami source of the Santa Cruz Islands earthquake. The coseismic rupture pattern (average model, Table S3) shows a main patch of slip (Fig. 4), located SE from the hypocenter, centred around $\sim 165.5^{\circ}\text{E}$ $\sim 11^{\circ}\text{S}$, and featuring a maximum slip value of ~ 11 m at a depth of ~ 25 km. The coseismic rupture reaches the shallowest portion of the subduction interface and it spreads along strike in NW direction with maximum slip values of ~ 6 m. The dislocation model resulting from the inversion shows a second smaller patch of slip located NW from the hypocenter and centred at a depth of ~ 29 km around $\sim 165^{\circ}\text{E}$ $\sim 10.5^{\circ}\text{S}$ (Fig. 4). This patch has a maximum slip of ~ 4 m. We found an average rake angle of $\sim 85^{\circ}$ in the easternmost part of the fault that is consistent with the relative convergence of the Australia and Pacific plates in this portion of the megathrust. On the other hand, the remaining part of the fault plane to the west is characterized by a slip angle lower than 50° . Hence, the dislocation there highlights a relevant strike-slip component, according with the change of the tectonic regime in this region, from purely thrust to left-lateral, as also shown by the regional seismicity. Figure 5 shows an overall good agreement between observed and predicted tsunami waveforms. During the inversion we applied a time shift (+2 min) to the Green's functions of Lata Wharf tide gauge due to the systematic anticipation of the predicted tsunami waveform with respect to the observed signal. This systematic difference between observed and predicted data is likely due to the relatively low accuracy of the nearshore bathymetry around this station. **We also proved the validity of the linearity assumption at the coastal tide**

gauges. The tsunami signals predicted with the time-shifted and linearly combined Green's functions are compared to the tsunami signals produced with a single forward run forced by the average slip model (Figure S4). This is in fair agreement with recent results of Yue et al. (2015).

The total seismic moment associated to the slip distribution resulting from the inversion, using a shear modulus equal to 30 GPa, is $M_0 = 1.033 \times 10^{21}$ Nm, that is equivalent to a moment magnitude $M_w = 8.0$ and in agreement with the estimations obtained from previous studies.

5 Discussion

5.1 Comparison with previous Santa Cruz Islands earthquake source models

In principle, teleseismic data well constrain the earthquake seismic moment and the seismic rupture history, and, compared to tsunami data, they are less sensitive to the spatial details of the slip distribution (e.g. Yue, 2014; Gusman et al., 2015). Moreover, adopting different fault geometries (and hypocenter) may result in different earthquake slip distributions (e.g. Baba et al., 2009; Hayes et al., 2014b). ~~The possibility of trade-off between the hypocentral depth, or the fault model, assumed during the inversion and both the resulting location and amount of slip is well known (e.g. Baba et al., 2009), with evident effects on the associated tsunami waves excitation.~~

The comparison among the present model, LA13, and HA14 shows some differences in terms of tsunami source that may be ascribed to the different data and fault model used in the inversions.

The slip model in this study, LA13, and HA14 models have been obtained using three different fault geometries (Fig. 6). Indeed, both LA13 and HA14 use a planar fault, whereas we adopt a 3D fault surface honouring the subduction zone interface. In addition, the fault in LA13 is overall shallower with respect to that in HA14, and LA13 also assumes a shallower hypocenter (~13 km, whereas it is ~29 km in HA14, compare Figs. 6b,d).

As shown in Lay et al. (2013), the slip distributions of the Santa Cruz Islands earthquake obtained by using only teleseismic data, adopting a hypocenter deeper than 15 km, and an overall deeper fault plane result in an under-prediction of tsunami observations at DART buoys. For this reason, Lay et al. (2013) prefer, among teleseismic solutions, the one obtained by imposing a shallower hypocenter. Since the model in this study and LA13

237 explain tsunami data to a similar extent, then the main differences between the two may be
238 ascribed either to differences in the adopted fault geometry, or to poor resolving power of
239 tsunami data themselves, which would lead to non uniqueness of the solution. According to
240 our synthetic test, the latter does not seem to be the case, at least as regards the most
241 tsunamigenic part of the source, that is the one with a dominant dip slip component in LA13
242 model. Besides this, we also may argue that the HA14 source, which shows a deeper slip
243 centroid than LA13 (and lower peak slip of about 4 m, Fig. 6a), should result less
244 tsunamigenic with respect to LA13 (peak slip > 10 m, Fig. 6c), and then likely
245 underestimate tsunami observations.

246 The centroid of the main asperity individuated in the present study is shifted SE with respect
247 to the main one of HA14 and it features quite larger slip (Fig. 6a). Conversely, it features
248 comparable peak slip values to the shallower patch in LA13 (Fig. 6c), but it is nearer to the
249 Nendo Island, as the two are only partially overlapped.

250 We also observe that the rake angle associated to our model is pretty consistent with the
251 relative convergence direction between Australia and Pacific plates. In particular, the slip
252 direction has behaviour close to a thrust-like motion (rake $\sim 85^\circ$) in the SE part of the fault
253 just nearby the northern-end of Vanuatu subduction zone; then the slip direction becomes
254 progressively more oblique highlighting a significant left-lateral component that is in
255 agreement with the kinematics (DeMets et al., 2010) and the seismicity of the NW segment
256 of the subduction (Fig. 1). On the other hand, we observe an opposite behaviour of the rake
257 angle in LA13; indeed, the southeastern shallower patch in LA13 has a slip direction with a
258 strong oblique component, whereas the northern deeper patch shows a thrust-like fault
259 motion. Thus, the main tsunamigenic patch in LA13 is located around the hypocenter,
260 whereas in the present study it is located in front of the Nendo Island, very close to the area
261 where the maximum tsunami wave heights have been observed (Fig. 1; Fritz et al., 2014;
262 NOAA/NGDC, http://www.ngdc.noaa.gov/hazard/tsu_db.shtml). Hence, as a likely less
263 tsunamigenic patch is involved, these differences may be due to a combination of the effects
264 of different resolving power of the data used and of different fault geometry.

265 In a further analysis, ~~we compare the rupture front that we imposed in the inversion with the~~
266 ~~resulting slip distribution;~~ we observe that $\sim 97\%$ of the total seismic moment ~~in our model is~~
267 ~~has been~~ released within 75 s from the nucleation. In particular, $\sim 60\%$ of the moment release
268 occurs ~~red~~ between 15 and 45 s, as ~~this~~ time window includes ~~ing~~ most of the main asperity
269 and the peak slip area (Fig. 4). Thus, ~~at least qualitatively, the moment rate we derive by~~
270 ~~combining the retrieved slip distribution and the imposed rupture velocity despite of the~~

~~differences among the models, and even though tsunami data are not particularly suitable to resolve the details of the seismic rupture history, our source model, at least at the first order,~~
is in agreement with the moment rate functions resulting from ~~studies that used~~ teleseismic ~~data~~ inversions.

5.2 Seismic rupture propagation SE from the hypocenter

The distribution of the early aftershocks (in the first 48h after the mainshock, <http://earthquake.usgs.gov/regional/neic/>), shows a lack of significant seismic events occurring at the subduction interface, a feature that might be indicative of a complete stress drop associated to the main February 6 event. On the other hand, a large number of seismic events have been observed mainly in the upper crust of the Pacific plate and in the eastern edge of the Australia plate oceanic crust (Fig. 4). In particular, the largest one in the Pacific plate (M_w 7+) occurred North of Nendo Island with a strike-slip right-lateral mechanism (Fig. 1) that is consistent with the kinematics of the coseismic slip (Hayes et al., 2014a). In addition, a cluster of shallow right-lateral aftershocks occurred SE from the mainshock epicenter (magenta ellipse in Fig. 4). In their study, Hayes et al. (2014a) propose that occurrence of these strike-slip earthquakes is caused by the block-like motion behaviour of the Pacific upper plate. However, they also argue that the Coulomb stress change distribution resulting from the HA14 coseismic model would promote events with left-lateral behaviour, whereas significant additional slip located SE from the hypocenter would promote the observed right-lateral aftershocks. They conclude that such slip (see magenta shaded ellipse in Fig. 6a), as not observed in HA14, then should be aseismic, should occur at the megathrust interface, and, in agreement with the Coulomb stress transfer estimation, should release a seismic moment of $M_0 = 3.1 \times 10^{20}$ Nm. Thus, the total (coseismic + aseismic) seismic moment released along the southeastern portion of the fault results to be $M_0 = 3.9 \times 10^{20}$ Nm. Noteworthy, our slip model is partially overlapped with the aseismic slip area argued by Hayes et al. (2014a); in particular, we observe larger slip values, up to 9 m confined in a smaller area, versus an average of 2 m of slip on a larger portion of the megathrust (Fig. 6a). The seismic moment associated to this portion of slip distribution in our model is $M_0 = 4.08 \times 10^{20}$ Nm, that is quite compatible with the estimation by Hayes et al. (2014a).

The location of the coseismic tsunami source that we found here is not in contradiction with the images of the rupture propagation resulting from back-projection analyses (IRIS, <http://ds.iris.edu/spud/backprojection/1065729>). Indeed, all of these analyses, while showing

different features depending on the seismic network employed, highlight a possible rupture propagation south-eastward from the hypocenter, shown as well by the slip models obtained using tsunami data (this study and LA13). Furthermore, on one hand in the back-projection analyses the surface projection of the radiated energy shows coherent high-frequency radiation along a portion of the megathrust corresponding to the seismogenic layer; on the other hand, the coherence of seismic high-frequency radiation appears to degrade south-eastward at shallower depths. This feature, along with the slip propagation up to the trench (a zone likely rich of sediments) and the relatively low rupture velocity (1.5 km/s, Lay et al., 2013) suggests that part of the seismic rupture SE of Nendo Island may have been characterized by slow slip, as indicated by Lay et al. (2013). Therefore, we cannot rule out that this portion of the megathrust, at least partially, may have slipped coseismically triggering the right-lateral strike-slip aftershocks.

6 Conclusion

We retrieved the coseismic tsunami source of the 2013 Santa Cruz Islands earthquake by inverting tsunami observations recorded in the Pacific Ocean by several DART buoys and tide gauges. We also computed the Green's functions using a 3D fault model honouring the geometrical complexities of the subduction interface. The retrieved coseismic tsunami source is mainly located SE from the hypocenter, with maximum slip value of ~11 m and with the coseismic rupture reaching the shallow part of the megathrust with slip amplitudes up to 6 m. The seismic moment resulting from our coseismic slip model is equivalent to an M_w 8.0 moment magnitude, in agreement with previous studies. The spatial pattern of the tsunami source is in agreement with the Australia and Pacific plates convergence direction that becomes progressively more oblique in the NW segment, and the slip distribution well reproduces the tsunami data. However, our model, compared with previously published models, features some differences in terms of tsunamigenesis and pattern of coseismic slip, that we have discussed in relation to the different resolving power of the data used and on the different fault geometry adopted. A common feature to all the models is the presence of slip SE from the hypocentre, which we argue to have occurred during the coseismic stage, possibly with a slow slip component, rather than being aseismic as previously suggested.

336 **Author contributions**

337 F.R. was involved in all of the phases of this study. I.M. built the 3D fault geometry,
338 processed tsunami data, and contributed to write the paper. S.L. and A.P. contributed to
339 design the experiment, to discuss and interpret the results and writing the paper. All authors
340 reviewed the final manuscript.

341

342

343 **Acknowledgments**

344 This work is partially funded by project ASTARTE - Assessment, Strategy And Risk
345 Reduction for Tsunamis in Europe - FP7-ENV2013 6.4-3, Grant 603839, and by the Italian
346 flagship project RITMARE. Some of the figures in this work were drawn using GMT
347 software (Wessel and Smith, 1995) and Matlab (<http://www.mathworks.it/products/matlab/>).

348

349 **References**

- 350 Aki, K.: Characterization of barriers on an earthquake fault, *J. Geophys. Res.*, 84,
351 6140-6148, 1979.
- 352
- 353 Baba, T., Cummins, P. R., Thio, H. K., and Tsushima, H.: Validation and Joint Inversion of
354 Teleseismic Waveforms for Earthquake Source Models Using Deep Ocean Bottom Pressure
355 records: A Case Study of the 2006 Kuril Megathrust Earthquake, *Pure Appl. Geophys.*, 166,
356 55-76, doi:10.1007/s00024-008-0438-1, 2009.
- 357
- 358 Barbosa, S. M., Fernandes, M. J., and Silva, M. E.: Nonlinear sea level trends from
359 European tide gauge records, *Ann. Geophys.*, 22, 1465–1472, doi:10.5194/angeo-22-1465-
360 2004, 2004.
- 361
- 362 Bird, P.: An updated digital model of plate boundaries, *Geochem. Geophys. Geosyst.*, 4,
363 1027, doi:10.1029/2001GC000252, 2003.
- 364
- 365 DeMets, C., Gordon, R. G., and Argus, D. F.: Geologically current plate motions, *Geophys.*
366 *J. Int.* 181, 1–80, doi:10.1111/j.1365-246X.2009.04491.x, 2010.
- 367
- 368 Engdahl, E.R., van der Hilst, R., and Buland, R.: Global teleseismic earthquake relocation
369 with improved travel times and procedures for depth determination, *Bull. Seism. Soc. Am.*,
370 88, 722-743, 1998.
- 371
- 372 Fritz, H. M., Papantoniou, A., Biukoto, L., Gilly, A., and Wei, Y.: The Solomon
373 Islands Tsunami of 6 February 2013 in the Santa Cruz Islands: Field Survey and
374 Modeling, EGU General Assembly 2014, held 27 April - 2 May, in Vienna, Austria,
375 id.15777, 2014.
- 376
- 377 Gusman, A. R., Murotani, S., Satake, K., Heidarzadeh, M., Gunawan, E., Watada, S.,
378 and Schurr, B.: Fault slip distribution of the 2014 Iquique, Chile, earthquake
379 estimated from ocean-wide tsunami waveforms and GPS data, *Geophys. Res. Lett.*,
380 42, doi:10.1002/2014GL062604, 2015.

381 Hayes, G.P., Wald, D.J., and Johnson, R.L.: Slab1.0: A three-dimensional model of
 382 global subduction zone geometries, *J. Geophys. Res.* 117, B01302,
 383 doi:10.1029/2011JB008524, 2012.
 384
 385 Hayes, G.P., Furlong, K.P., Benz, H.M., and Herman, H.W.: Triggered aseismic slip
 386 adjacent to the 6 February 2013 Mw8.0 Santa Cruz Islands megathrust earthquake,
 387 *Earth Planet. Sci. Lett.* 388, 265-272, doi: 10.1016/j.epsl.2013.11.010, 2014a.
 388
 389 Hayes, G.P., Herman, M. W., Banhart, W. D., Furlong, K. P., Riquelme, S., Benz, H.M.,
 390 Bergman, E., Barrientos, S., Earle, P. S., and Samsonov, S.: Continuing megathrust
 391 earthquake potential in Chile after the 2014 Iquique earthquake, *Nature* 512, 295–298,
 392 doi:10.1038/nature13677, 2014b.
 393
 394 Lay, T., Ye, L., Kanamori, H., Yamazaki, Y., Cheung, K.F., and Ammon, C.J.: The
 395 February 6, 2013 Mw 8.0 Santa Cruz Islands earthquake and tsunami, *Tectonophysics*, 608,
 396 1109-1121, doi:10.1016/j.tecto.2013.07.001, 2013.
 397
 398 Lorito, S., Romano, F., Atzori, S., Tong, X., Avallone, A., McCloskey, J., Cocco, M.,
 399 Boschi, E., and Piatanesi, A.: Limited overlap between the seismic gap and coseismic slip of
 400 the great 2010 Chile earthquake, *Nature Geosci.*, 4(3), 173-177, doi:10.1038/NGEO1073,
 401 2011.
 402
 403 Meade, B. J.: Algorithms for the calculation of exact displacements, strains, and stresses for
 404 triangular dislocation elements in a uniform elastic half space, *Comput. Geosci.* 33, 1064-
 405 1075, doi:10.1016/j.cageo.2006.12.003, 2007.
 406
 407 Piatanesi, A., and Lorito, S.: Rupture process of the 2004 Sumatra-Andaman earthquake
 408 from tsunami waveform inversion, *Bull. Seismol. Soc. Am.*, 97(1), 223-231,
 409 doi:10.1785/0120050627, 2007.
 410
 411 Romano, F., Piatanesi A., Lorito, S., D'Agostino, N., Hirata, K., Atzori, S., Yamazaki, Y.,
 412 and Cocco, M.: Clues from joint inversion of tsunami and geodetic data of the 2011 Tohoku-
 413 oki earthquake, *Sci. Rep.* 2, 385; DOI:10.1038/srep00385, 2012.
 414

415 Romano, F., Trasatti, E., Lorito, S., Piromallo, C., Piatanesi, A., Ito, Y., Zhao, D.,
 416 Hirata, K., Lanucara, P., and Cocco, M.: Structural control on the Tohoku earthquake
 417 rupture process investigated by 3D FEM, tsunami and geodetic data, *Sci. Rep.*, 4,
 418 5631, doi:10.1038/srep05631, 2014.
 419
 420 Rothman, D.: Automatic estimation of large residual statics corrections, *Geophysics* 51,
 421 332–346, doi:10.1190/1.1442092, 1986.
 422
 423 Spudich, P., and Miller, D. P.: Seismic site effects and the spatial interpolation of earthquake
 424 seismograms: results using aftershocks of the 1986 North Palm Springs, California,
 425 earthquake, *Bull. Seismol. Soc. Am.* 80, 6, 1504–1532, 1990.
 426
 427 Tanioka, Y., and Satake, K.: Tsunami generation by horizontal displacement of ocean
 428 bottom, *Geophys. Res. Lett.* 23, 8, 861–864, doi:10.1029/96GL00736, 1996.
 429
 430 Wessel, P., and Smith, W. H. F.: New version of the Generic Map- ping Tools
 431 released, *Eos Trans. AGU*, 76, 329, doi:10.1029/95EO00198, 1995.
 432
 433 Yamazaki, Y., Kowalik, Z., and Cheung, K. F.: Depth-integrated, non-hydrostatic model for
 434 wave breaking, *Int. J. Numer. Meth. Fluids*, 61, 473–497, doi:10.1002/fld.1952, 2009.
 435
 436 Yamazaki, Y., Cheung, K. F., and Kowalik, Z.: Depth-integrated, non-hydrostatic model
 437 with grid nesting for tsunami generation, propagation, and run-up, *Int. J. Numer. Meth.*
 438 *Fluids*, 67, 2081–2107, doi:10.1002/fld.2485, 2011.
 439
 440 Yue, H: Toward resolving stable high-resolution kinematic rupture models of large
 441 earthquakes by joint inversion of seismic, geodetic and tsunami observations, PhD
 442 Thesis, 2014.
 443
 444 Yue, H., Lay, T., Li, L., Yamazaki, Y., Cheung, K.F., Rivera, L., Hill, E.M., Sieh,
 445 K., Kongko, W., and Muhari, A.: Validation of linearity assumptions for using
 446 tsunami waveforms in joint inversion of kinematic rupture models: Application to the
 447 2010 Mentawai Mw 7.8 tsunami earthquake, *J. Geophys. Res.*, 120, 1728–1747,
 448 doi:10.1002/2014JB011721, 2015.

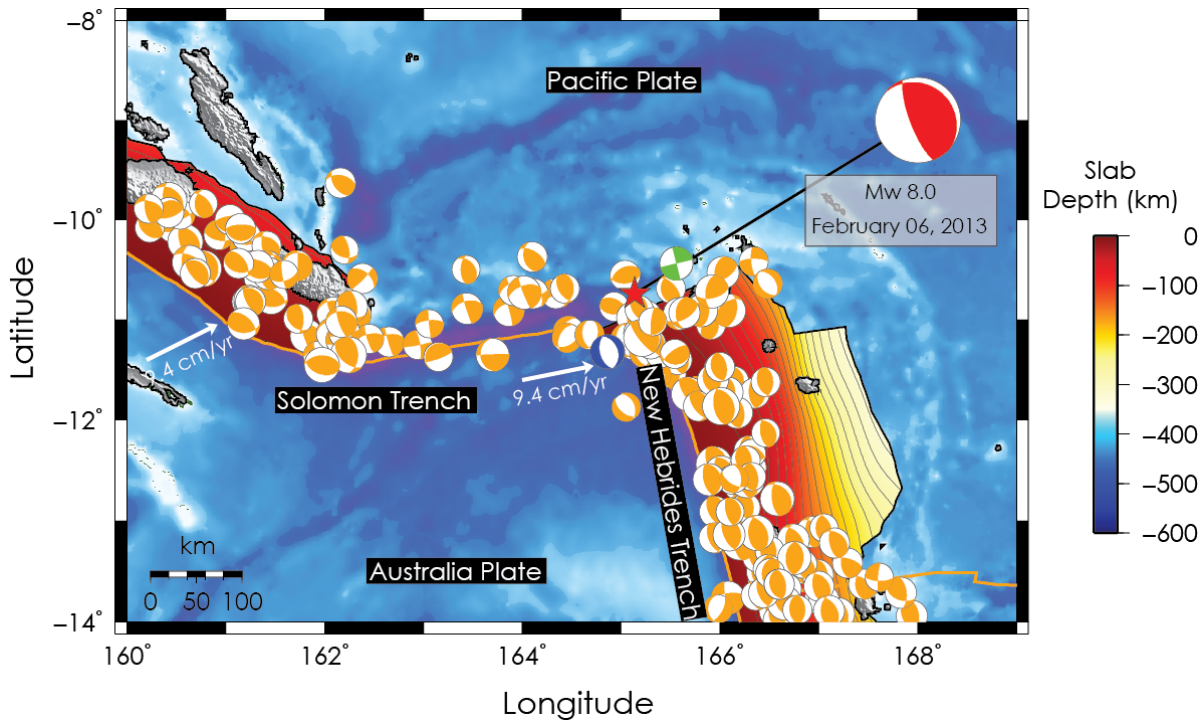


Figure 1 – Location map of the 2013 Santa Cruz Islands earthquake. Red star and red beach ball indicate epicenter and focal mechanism of the mainshock, respectively. Green and blue beach balls indicate the focal mechanisms of the largest strike-slip (M_w 7.0) and normal (M_w 7.1) aftershocks occurred few hours after the mainshock. Orange beach balls indicate the regional historical seismicity (since 1976 to present, GCMT catalogue, <http://www.globalcmt.org/CMTsearch.html>) and the corresponding focal mechanisms for earthquake magnitude 6+. White arrows indicate the convergence direction of the Australia Plate.

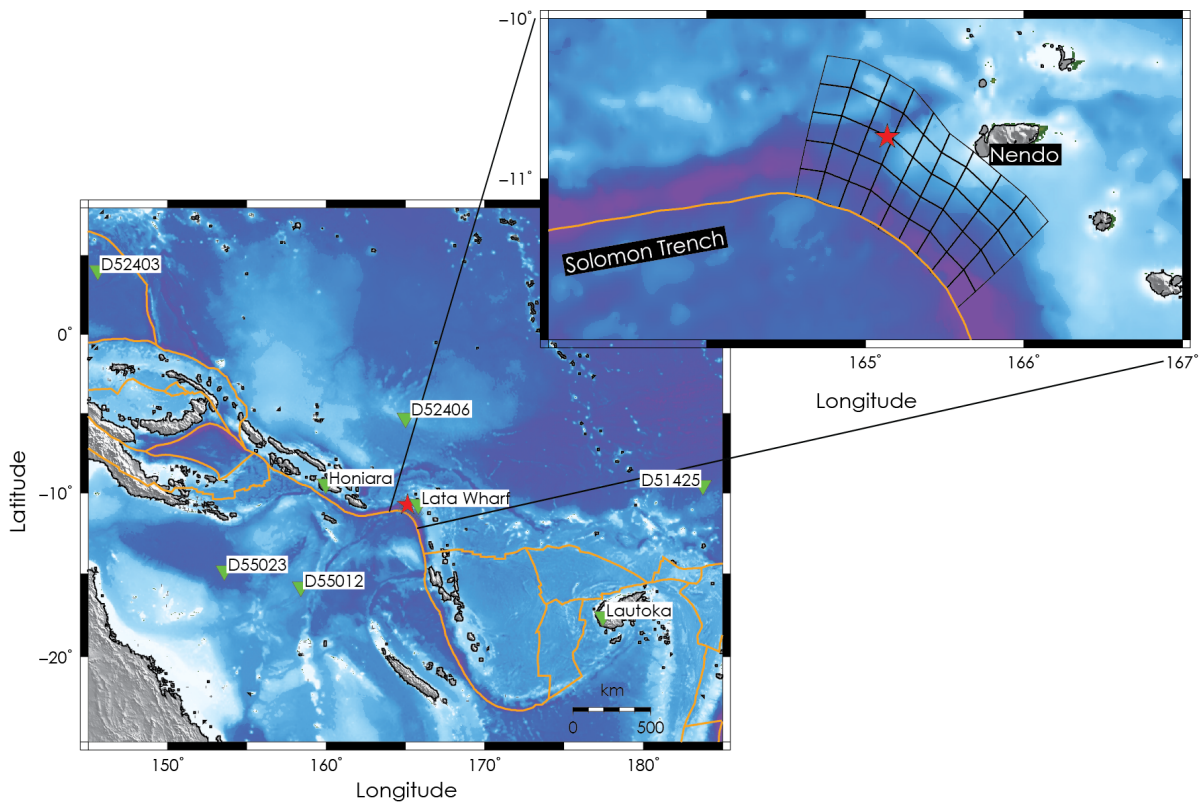


Figure 2 – Data and fault model. Green triangles indicate DART buoys and tide gauges used in this study. The top-right panel is a close-up view of the fault model adopted. Red star indicates the Santa Cruz Islands earthquake epicenter.

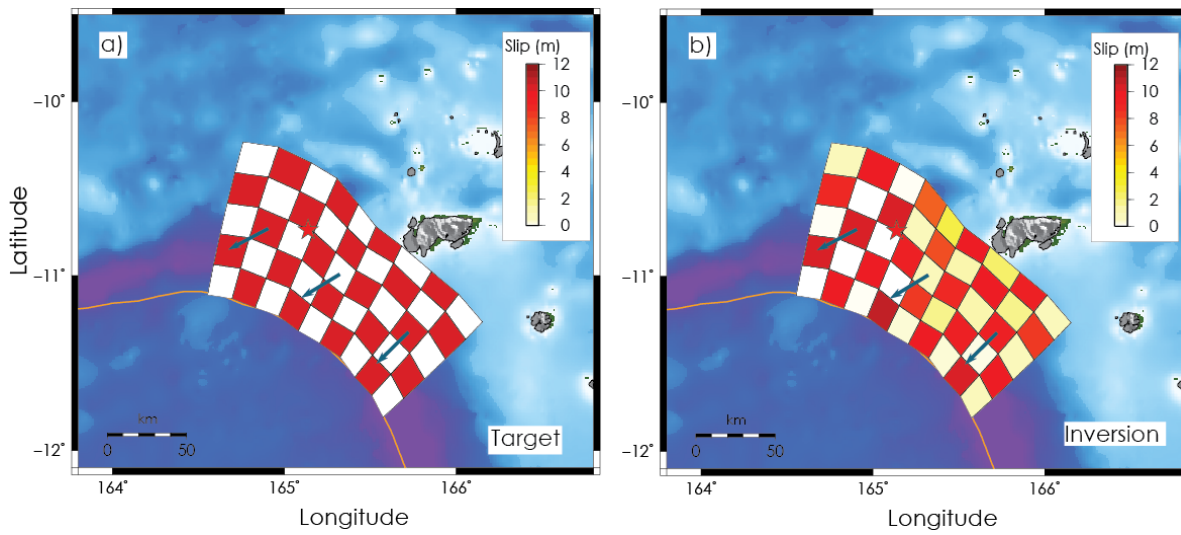


Figure 3 – Resolution test. a) Target slip and rake (blue arrows) pattern; b) slip model obtained inverting tsunami data.

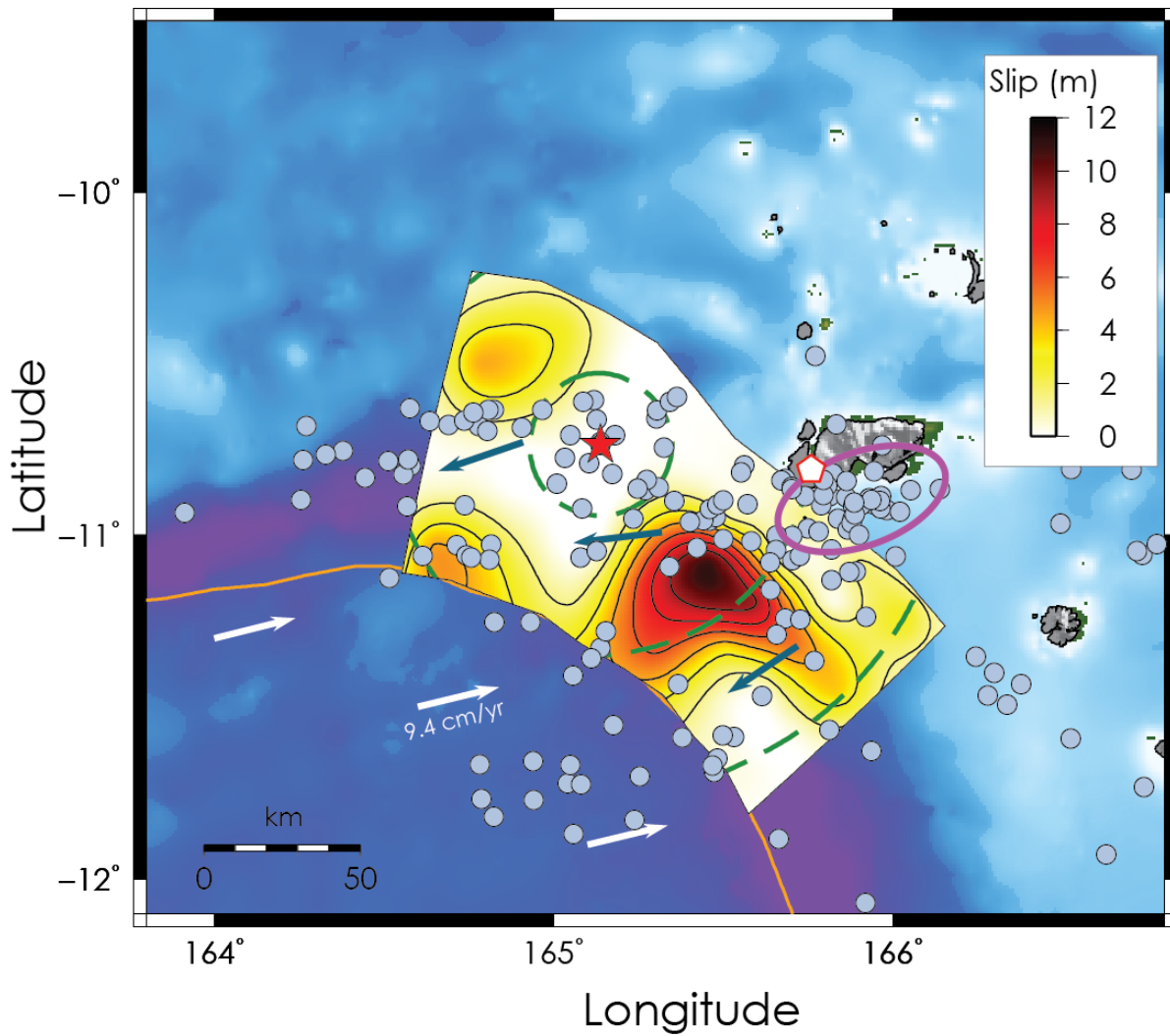


Figure 4 – Coseismic tsunami source of the 2013 Santa Cruz Islands earthquake. Slip model is contoured (black solid line) in 1.5 m intervals. Blue arrows indicate the rake. White arrows indicate the convergence direction of the Australian Plate. Cyan dots represent the early aftershocks (occurred by 48 hours after the mainshock, NEIC catalogue). Magenta ellipse approximately indicates the cluster of right-lateral strike-slip aftershock events. White pentagon indicates the area where have been observed the maximum tsunami wave heights (Fritz et al., 2014; NOAA/NGDC, http://www.ngdc.noaa.gov/hazard/tsu_db.shtml). Green dashed circles represent the rupture front expansion (rupture velocity 1.5 km/s) at 15, 45, and 75 s.

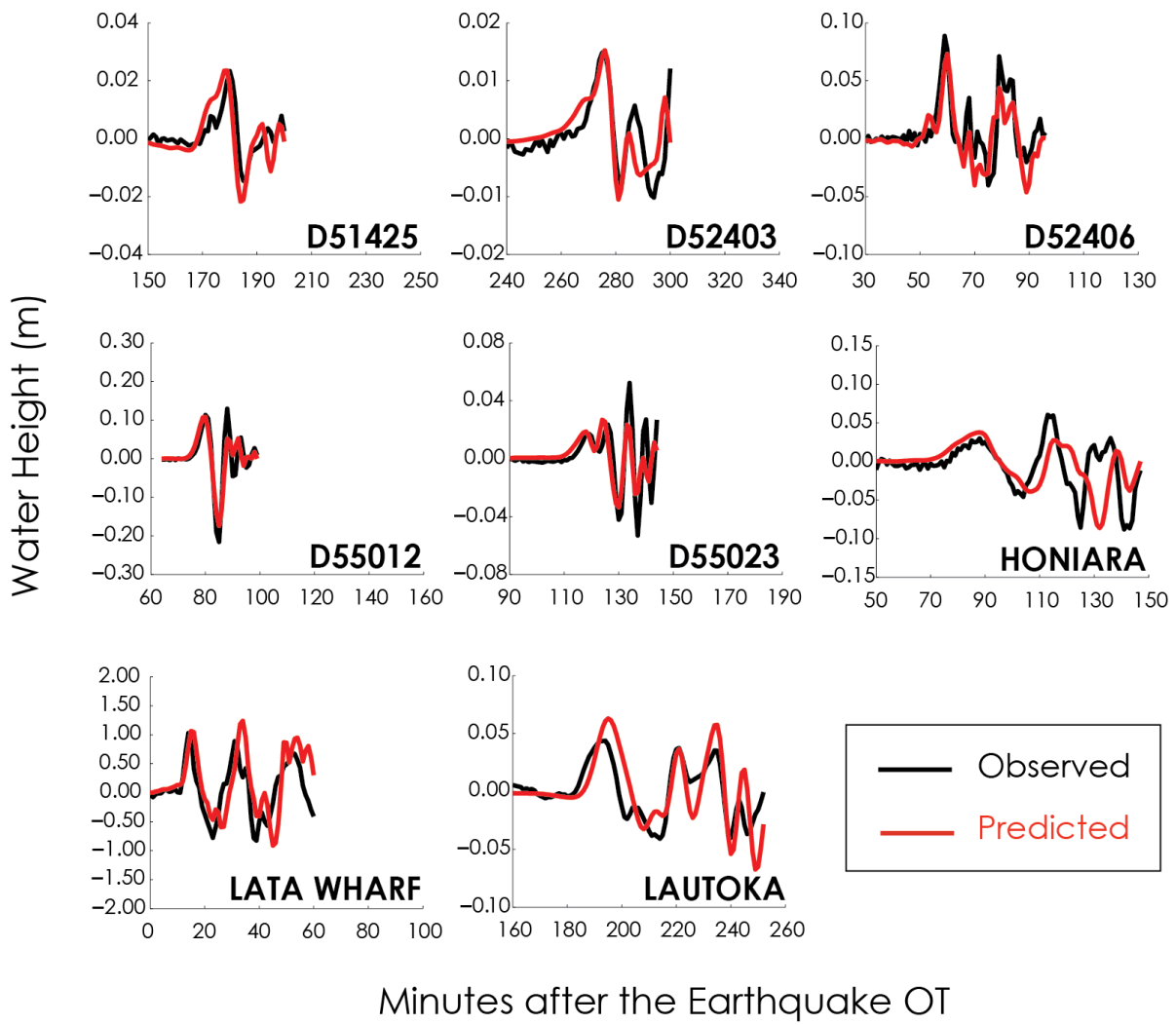


Figure 5 – Data fit. Comparison between observed (black) and predicted (red) tsunami data.

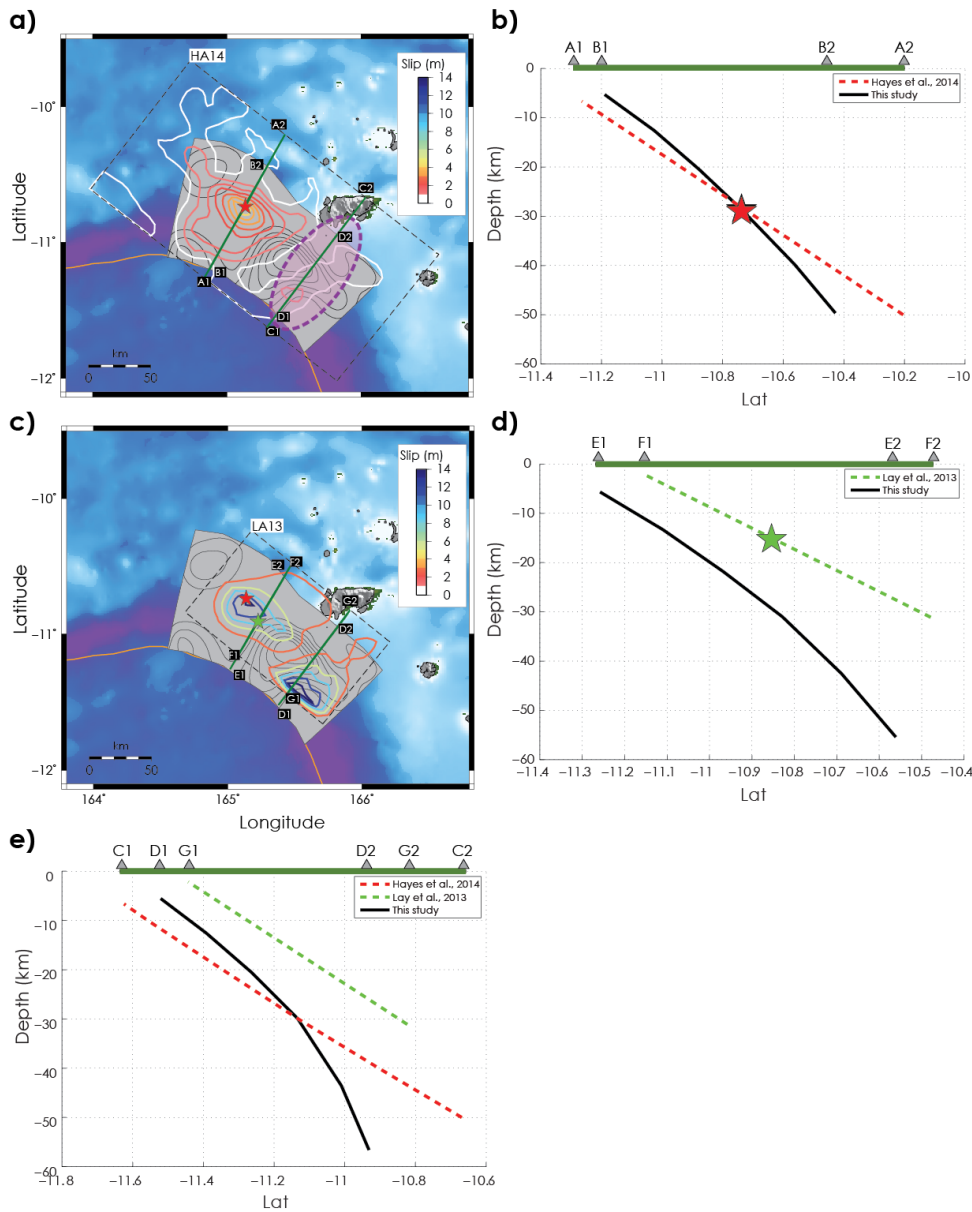


Figure 6 – Comparison with other source models. a) HA14 model (coloured solid lines at 0.5 m intervals); magenta ellipse approximately represents the aseismic slip area hypothesized in HA14; black solid lines as in Figure 4; green solid lines represent the surface projections of the depth profiles along the HA14 fault model and that one adopted in this study. b) Depth profiles along the HA14 fault model (red) and that one adopted in this study (black) crossing the hypocenter used in HA14 (red star) and in this study (black star); notice that the two hypocenters are almost coincident. c) LA13 model (coloured solid lines at 2.8 m intervals); black solid lines as in Figure 4; green solid lines represent the surface projections of the depth profiles along the LA13 fault model and that one adopted in this study. d) Depth profiles along the LA13 fault model (green) and that one adopted in this study (black) crossing the hypocenter used in LA13 (green star) ~~and in this study (black~~

499 | ~~star~~. e) Depth profiles along the LA13 and HA14 fault models and that one adopted in this
500 study crossing the aseismic slip area hypothesized in HA14.